Research Article | Open Access

Soft Science

Lei *et al. Soft Sci.* **2026**, *6*, 41 **DOI:**10.20517/ss.2026.22

Wearable PANI@$CoFe_2O_4$ organohydroges for strain sensing, EMI shielding and thermal insulation

Zhi Lei, Maoxia Lu, Daohai Zhang*, Dongju Liu, Yupeng Hu, Anmin Song, Junlei Wang, Wei Gong

Keywords:
Multifunctional materials, hydrogels, electromagnetic shielding, wearable devices

Citation: Lei, Z.; Lu, M.; Zhang, D.; Liu, D.; Hu, Y.; Song, A.; Wang, J.; Gong, W. Wearable PANI@$CoFe_2O_4$ organohydroges for strain sensing, EMI shielding and thermal insulation. *Soft Sci.* **2026**, *6*, 41. https://dx.doi.org/10.20517/ss.2026.22

Received: 28 Jan 2026
First Decision: 25 Feb 2026
Revised: 15 Mar 2026
Accepted: 26 Mar 2026
Published: 20 May 2026

Academic Editor:
Junwei Gu
Copy Editor:
Shu-Yuan Duan
Production Editor:
Shu-Yuan Duan

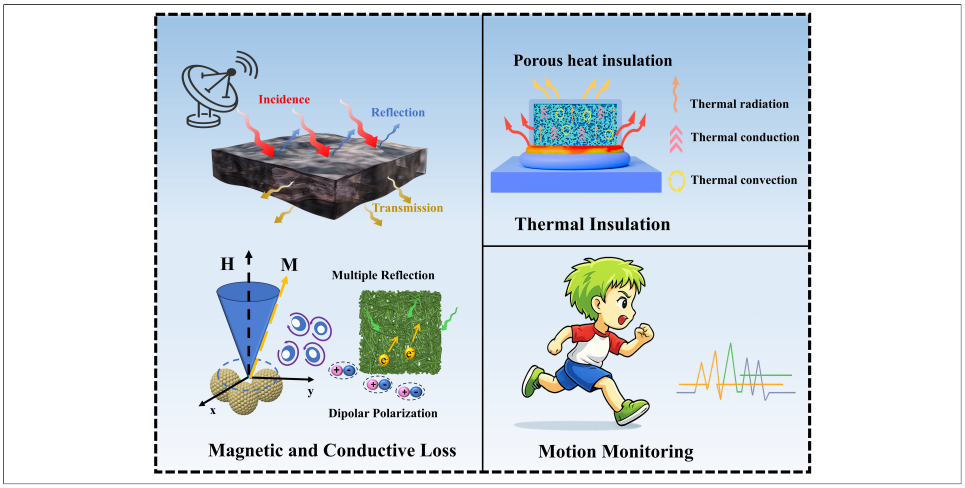

Abstract

With the rapid escalation of electromagnetic pollution and electromagnetic interference, conventional EMI shielding materials can no longer satisfy the integrated requirements of next-generation flexible electronic devices and information terminals for mechanical deformability, wearable adaptability, and real-time signal monitoring. In this work, a multifunctional polyacrylamide/glycerol (PG)/P@CoFe (PAM/Gly/PANI@$CoFe_2O_4$) composite organohydrogel sensor with synergistic electromagnetic dissipation was fabricated through a hydrothermal-assisted one-pot strategy. $CoFe_2O_4$ magnetic nanoparticles were first synthesized via an ethylene glycol-assisted solvothermal route. Subsequently, the surface-active sites of $CoFe_2O_4$ were utilized to induce aniline polymerization, yielding conductive-magnetic polyaniline (PANI)@$CoFe_2O_4$ composite nanoparticles. Mechanical characterization demonstrated that the resulting organohydrogel exhibited excellent compressive properties, while the incorporation of glycerol effectively suppressed water evaporation and enhanced water-retention capability. Electromagnetic measurements revealed that, at a PANI@$CoFe_2O_4$ loading of 4 wt.%, the 4 mm-thick hydrogel achieved an electrical conductivity of 0.55 ± 0.01 S/m and an average electromagnetic interference shielding effectiveness (EMI SE) of 50.27 ± 2.51 dB in the X-band. In addition, the hydrogel exhibited excellent thermal iInsulation performance. More importantly, its outstanding adhesion and rapid stimuli-responsive behavior enabled

School of Chemical Engineering of Guizhou Minzu University, Guiyang 550025, Guizhou, China.

*Correspondence to: Prof. Daohai Zhang. School of Chemical Engineering of Guizhou Minzu University, Guiyang 550025, Guizhou, China. E-mail: zhangdaohai6235@163.com

favorable human-machine interactive strain-sensing performance with good compatibility. This work provides an effective strategy for the development of integrated, robust multifunctional materials that simultaneously combine flexible sensing, electromagnetic shielding, and thermal insulation.

Highlights

1. A multifunctional PG/P@CoFe organohydrogel was fabricated via a hydrothermal-assisted one-pot strategy.
2. *In situ* polymerized PANI uniformly coated $CoFe_2O_4$, forming a stable conductive-magnetic synergistic network.
3. The organohydrogel exhibited high-sensitivity strain sensing together with favorable infrared stealth performance.
4. Absorption-dominated EMI shielding is achieved with an average SE of 50.27 dB in the X-band.

INTRODUCTION

With the rapid development of 5G communications, artificial intelligence, and aerospace technologies, the problems of electromagnetic pollution and electromagnetic interference have become increasingly serious, threatening the stable operation of precision electronic devices and raising potential concerns for human health[1-4]. Conventional electromagnetic shielding materials are primarily designed to attenuate incident electromagnetic waves. however, they are increasingly unable to satisfy the growing demand for lightweight design, flexibility, and multifunctional integration required by emerging applications such as internet-connected devices, wearable electronics, and health monitoring systems[5-7]. As electronic devices become increasingly miniaturized and sophisticated, and as their application scenarios become more complex, the development of EMI shielding materials must evolve toward multifunctional integration[8-10]. Owing to their lightweight nature, mechanical softness, inherent adhesiveness, and excellent compatibility with functional fillers, hydrogels have emerged as highly promising candidates for this purpose[11-13]. Through rational engineering of the polymeric network and precise regulation of functional fillers, their physicochemical properties and application-specific functionalities can be effectively tailored. By incorporating various conductive fillers, such as conductive polymers, carbon nanotubes, graphene, and metal-based materials, the electrical conductivity of hydrogels can be effectively regulated[14,15]. This unique combination has made hydrogels highly attractive for applications in flexible electronics, energy storage and sensing, while also offering a new framework for the development of multifunctional and integrated electromagnetic shielding materials. However, a critical challenge remains. Most conductive fillers exhibit poor dispersibility in hydrogel precursor solutions and tend to aggregate or sediment. Therefore, the rational selection and surface modification of functional fillers are crucial for constructing high-performance composite hydrogels.

Among various conducting polymers, polyaniline (PANI) has attracted extensive attention owing to its tunable oxidation states, high electrical conductivity, and capability for in situ polymerization in aqueous media[16]. However, pristine PANI exhibits strong hydrophobicity and limited hydrophilicity, resulting in poor solubility and unsatisfactory dispersibility in aqueous systems. In acidic media, protonation of the PANI molecular chains can markedly improve both its dispersibility and electrical conductivity[17,18]. Nevertheless, excessively high electrical conductivity can easily lead to discontinuous conductive pathways and a limited number of interfacial polarization sites, resulting in unsatisfactory electromagnetic wave attenuation performance[19]. Therefore, it is necessary to introduce other components to alleviate issues such as insufficient interfacial polarization. $CoFe_2O_4$ is a typical spinel-structured magnetic material and a ferrite that possesses high magnetic anisotropy, considerable magnetostrictive properties, and strong electromagnetic loss capability[20,21]. $CoFe_2O_4$ exhibits excellent thermochemical stability, enabling it to

maintain its structural integrity without significant decomposition even under acidic, oxidizing, or high-temperature conditions[22-24]. Unfortunately, its electrical conductivity is inferior compared with that of many metal-based materials[25,26]. It is predominantly employed as a magnetic loss component rather than a highly conductive material in electromagnetic shielding and microwave absorption applications. Wang *et al.*[5] prepared the MXene/$CoFe_2O_4$ multifunctional hydrogel via a rapid gelation method, which not only addressed the issue of filler agglomeration but also improved the electrical conductivity of the hydrogel. The average EMI SE of this hydrogel in the X-band reaches 54.21 dB. Zhou *et al.*[27] prepared Fe_3O_4@RGO by a hydrothermal method, which resolved the problems of Fe_3O_4 precipitation and RGO stacking. They also fabricated the Fe_3O_4@RGO/PAM conductive hydrogel, whose maximum EMI SE is 27.1 dB. Diao *et al.*[11] optimized MXene layers via covalent organic frameworks (COFs) and successfully prepared MXene@COF heterostructured hydrogels, preventing MXene nanosheets from aggregation and self-stacking through the outer layer. The average EMI SE of this hydrogel is 32.01 dB. Thus, we can effectively overcome their respective defects by compounding PANI conductive materials and $CoFe_2O_4$ magnetic materials: On the one hand, the magnetic particles contribute magnetic loss mechanisms such as natural resonance and eddy current loss[20,28,29]. On the other hand, the interfaces between $CoFe_2O_4$ and PANI can induce dipole polarization and interfacial polarization, thereby enabling a synergistic multi-mechanism attenuation of electromagnetic waves[30,31]. More importantly, the integration of the conductive PANI network with magnetic $CoFe_2O_4$ nanoparticles facilitates the construction of a composite network that simultaneously exhibits dielectric and magnetic loss characteristics, thereby optimizing impedance matching and enhancing the overall microwave absorption efficiency. In addition, polyacrylamide (PAM), as a hydrophilic polymer network material, possesses excellent flexibility and a controllable porous structure, making it an ideal matrix for constructing composite hydrogels[32-34]. The incorporation of glycerol (Gly) not only significantly enhances the mechanical toughness and water-retention capability of the hydrogel, but also promotes internal energy dissipation and stabilizes the conductive network through hydrogen-bond interactions.

In this work, we successfully synthesized $CoFe_2O_4$ magnetic nanoparticles via a hydrothermal method. Owing to the abundant surface metal active sites (Co^{2+} and Fe^{3+}), surface hydroxyl groups (-OH), and oxygen vacancies, the nanoparticles exhibit a strong adsorption capability toward aniline[35]. The lone-pair electrons on the amino group of aniline can coordinate with Co^{2+} and Fe^{+}, enriching aniline at the $CoFe_2O_4$ surface and facilitating subsequent in situ oxidative polymerization. This interfacial coordination is the key to constructing conductive-magnetic PANI@$CoFe_2O_4$ composite nanoparticles. Based on this mechanism, the homogeneous incorporation of PANI@$CoFe_2O_4$ into the polyacrylamide/glycerol (PG) (PAM/Gly) matrix enables the construction of a hierarchical conductive–magnetic synergistic network, thereby endowing the hydrogel with integrated EMI shielding, thermal insulation, and flexible strain-sensing properties.

EXPERIMENTAL SECTION

Experimental materials

Cobalt(II) chloride hexahydrate ($CoCl_2·6H_2O$, reagent grade, 99.9%, molecular weight 291.03), ferric chloride hexahydrate ($FeCl_3·6H_2O$, analytically pure, 99%, molecular weight 270.30), acrylamide (AM, analytically pure, 99.0%, molecular weight 71.08), ammonium persulfate (APS, analytically pure, 98%, molecular weight 228.20), N,N′-methylenebisacrylamide (MBA, 99%, molecular weight 154.17), sodium hydroxide (NaOH, analytically pure, 96.0%, molecular weight 40.00) were all purchased from Shanghai Aladdin Biochemical Technology Co., Ltd. Aniline (AN, ≥ 99.5%, molecular weight 93.13), hydrochloric acid (HCl, 36.5-38.0 wt.%, molecular weight 36.46) and ethylene glycol (EG, analytically pure, ≥ 98%, molecular weight 62.07) were purchased from Chongqing Chuandong Chemical Co., Ltd. Glycerol (Gly, analytically pure, ≥ 99.0%, molecular weight 92.09) was purchased from Xilong Scientific Co., Ltd.

Preparation of conductive and magnetic PANI@$CoFe_2O_4$ nanoparticles

Take a certain mass of $CoCl_2 \cdot 6H_2O$ and $FeCl_3 \cdot 6H_2O$ and dissolve them sequentially in 45 mL of ethylene glycol to form solution a. Then dissolve NaOH in 50 mL of ethylene glycol to form solution b. Slowly add a to b while stirring magnetically in a 50 °C water bath for 2 h; Next, react it in a reactor at 200 °C for 8 h. After centrifugation, washing, and drying, $CoFe_2O_4$ magnetic particles are obtained.

Disperse $CoFe_2O_4$ nanoparticles in 75 mL of deionized water, then add 0.1 mL of AN and stir for 20 min. Adjust the pH to 1 using HCl, then add the initiator APS. The mixture was stirred at 0-4 °C for 6 h, followed by centrifugation, washing, and drying to obtain PANI@$CoFe_2O_4$ conductive magnetic nanoparticles.

Preparation of PG/P@CoFe hydrogel

A specified amount of PANI@$CoFe_2O_4$ was dispersed in 100 mL of deionized water and uniformly homogenized by mechanical stirring. Subsequently, 8 g of acrylamide (AM), 1.9 mL of glycerol (Gly), and 0.08 g of N,N′-methylenebisacrylamide (MBA) were sequentially introduced into the PANI@$CoFe_2O_4$ dispersion and thoroughly mixed. The polymerization initiator, ammonium persulfate (APS, 0.195 g), was then added to the mixture, and the resulting solution was transferred into a custom-designed mold for gelation. The obtained hydrogel was designated as X-PG/P@CoFe, where PG denotes the PAM/Gly network, and X indicates the weight percentage (%) of PANI@$CoFe_2O_4$ filler incorporated into the hydrogel.

Characterization and measurements

Sample microstructures were examined by scanning electron microscopy (SEM, ZEISS Sigma 300, Carl Zeiss AG). Chemical composition was analyzed via Fourier transform infrared spectroscopy (FT-IR, Nicolet iS50, Thermo Fisher Scientific) and X-ray photoelectron spectroscopy (XPS, Thermo Scientific K-Alpha, Thermo Fisher Scientific), and crystal structures were determined by X-ray diffraction (XRD, Rigaku Ultima IV, Suzhou Dehe Scientific Instrument Co., Ltd). Thermal behavior of the hydrogels was assessed using differential scanning calorimetry (DSC, Q10, TA Instruments), while compressive properties were measured with an electronic universal testing machine (GB/T 1041-2008, CMT6104， Mettler Industrial Systems (China) Co., Ltd.). Water absorption (Q) and retention (W) capacities were quantified according to Equations (1) and (2)[11].

$$Q = \frac{m_t - m_0}{m_0} \times 100\% \tag{1}$$

$$W = \frac{w_t}{w_0} \times 100\% \tag{2}$$

Here, m_t denotes the weight of the sample in its original state, m_0 denotes the weight of the sample in a dry state; w_t denotes the mass measured after exposure to air for t h, and w_0 denotes the mass immediately upon reaching swelling equilibrium. Using a flexible strain sensor for sensitivity performance testing, the sensitivity coefficient (GF) is defined as the relative change in resistance [expressed as $(R\text{-}R_0)/R_0$, where R and R represent the initial and real-time resistance] divided by the strain (ε). The electrical conductivity of the samples was determined using a standard four-probe resistance tester (FT-331). Using a vector network analyzer (N5225B, Keysight, Malaysia), the scattering parameters (S11, S12, S21, and S22), along with the complex permittivity and complex susceptibility used for analyzing EMI shielding characteristics. EMI shielding performance, including total SET, reflected SER, and absorbed SEA, as well as the coefficients for reflectance (R), absorptance (A), and transmittance (T), is calculated using the following Equations (3) to (8)[36,37].

$$R = |S_{11}|^2 \tag{3}$$

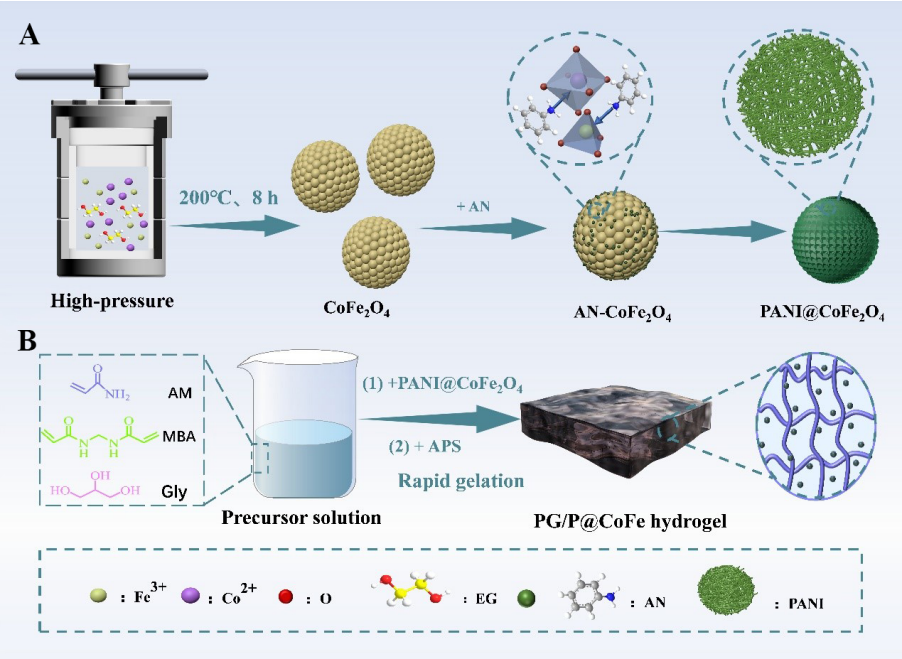

Figure 1. Preparation flowchart of the PG/P@CoFe hydrogel. PG: Polyacrylamide/glycerol; EG: Ethylene glycol; AN: Aniline; PANI: Polyaniline; MBA: N,N′-methylenebisacrylamide; Gly: Glycerol; AM: acrylamide; APS: ammonium persulfate.

$$T = |S_{21}|^2 \tag{4}$$

$$A = 1 - T - R \tag{5}$$

$$SE_R = 10 \log \frac{1}{T} \tag{6}$$

$$SE_A = 10 \log \frac{1 - R}{T} \tag{7}$$

$$SE_T = SE_R + SE_A \tag{8}$$

Statistical analysis

Normality was assessed using the Shapiro-Wilk test prior to parametric analysis. Given the small sample size (n = 3), the data were considered approximately normally distributed. Descriptive statistics were calculated for all datasets. Quantitative data are expressed as mean ± standard deviation (SD). Comparisons between two groups were performed using an unpaired two-tailed t-test. Statistical significance was defined as $P < 0.05$. All statistical calculations were performed using Origin 2021.

RESULTS AND DISCUSSION

Synthesis mechanism and microstructure of PANI@$CoFe_2O_4$ and PG hydrogels

As illustrated in Figure 1A, ethylene glycol promoted the nucleation and crystal growth of $CoFe_2O_4$ and facilitated the formation of the spinel phase. The abundant surface metal-active sites of $CoFe_2O_4$ can coordinate with the amino nitrogen of aniline, thereby enriching aniline at the particle interface and favoring subsequent interfacial oxidative polymerization. Upon initiation by APS, aniline polymerized to form PANI, which coated the $CoFe_2O_4$ surface to yield the PANI@$CoFe_2O_4$ composite. Subsequently, as shown in Figure 1B, the composite was introduced into the Gly/PAM precursor solution and underwent in situ gelation, resulting in the formation of the PANI@$CoFe_2O_4$ hydrogel.

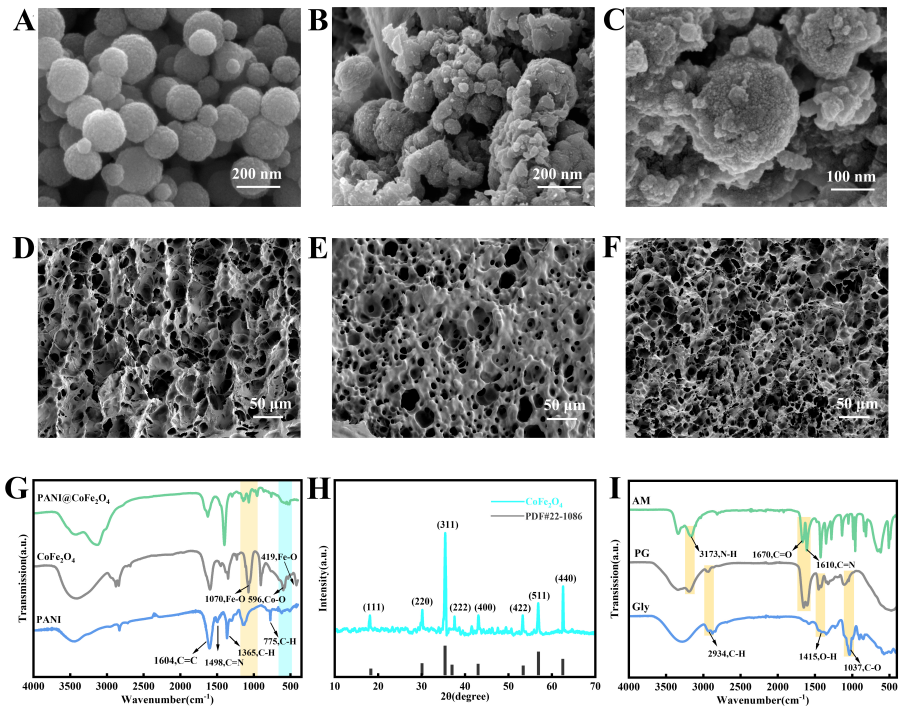

Figure 2. Microstructure and spectroscopic characterization of PANI@$CoFe_2O_4$ and PG-based hydrogels; (A) SEM images of $CoFe_2O_4$; (B and C) SEM images of PANI@$CoFe_2O_4$; (D-F) SEM images of PG, 4-PG/PANI, and 4-PG/P@CoFe; (G) FTIR spectra of PANI, $CoFe_2O_4$, and PANI@$CoFe_2O_4$; (H) XRD pattern of $CoFe_2O_4$; (I) FTIR spectrum of the PG hydrogel. AM: Acrylamide; PG: polyacrylamide/glycerol; SEM: scanning electron microscopy; FTIR: Fourier transform infrared; XRD: X-ray diffraction.

As shown in Figure 2A, the $CoFe_2O_4$ synthesized in ethylene glycol exhibits a relatively uniform spherical morphology. After compositing with PANI in the aqueous phase [Figure 2B and C], the $CoFe_2O_4$ particles were clearly encapsulated by a PANI coating layer. EDS elemental mapping and energy-dispersive spectroscopy analysis [Supplementary Figure 1] further confirmed the homogeneous distribution of C, N, Fe, and Co throughout the composite. Figure 2D-F shows the scanning electron microscopy image of the PG hydrogel, which exhibits a well-defined three-dimensional porous structure. When $CoFe_2O_4$ is introduced into the PG hydrogel, the pore structure of the hydrogel is disrupted [Figure 2E]. This phenomenon may be attributed to the aggregation and deposition of $CoFe_2O_4$ particles, which interact strongly with the polymer matrix. Such interactions lead to a tighter packing of the polymer chains, thereby reducing the size of the pore structures[38,39]. In contrast, when PANI@$CoFe_2O_4$ is incorporated, the pore structure becomes more abundant [Figure 2F]. The FTIR spectrum [Figure 2G] shows that the in situ polymerized PANI under acidic conditions exhibits a stretching vibration of the C=C bond at 1,604 cm^{-1}, a stretching vibration of the C-N bond at 1,498 cm^{-1}, and bending vibrations of the C-H bonds in the aromatic ring at 1,365 cm^{-1} and 775 cm^{-1}, as well as out-of-plane bending vibrations[40,41]. For $CoFe_2O_4$, the stretching vibration peaks of the Fe-O bonds appear at 419 cm^{-1} and 1,070 cm^{-1}, while the stretching vibration of the Co-O bond is observed at 596 cm^{-1}[42-44]. For the PANI@$CoFe_2O_4$ composite material, the characteristic peaks at 1,070 cm^{-1} and 596 cm^{-1} remain, indicating that the Fe-O and Co-O bonds are still present in the composite. Additionally, the peaks corresponding to PANI can also be observed, indicating the successful integration of PANI with $CoFe_2O_4$. Meanwhile, at the same time, as shown in Figure 2H, the diffraction peaks corresponding to each crystal face in the spinel structure perfectly match those in the standard card (No. 22-1086)[45], confirming the successful synthesis of the $CoFe_2O_4$ spinel structure. PG organohydroges were prepared using glycerol (Gly) and acrylamide (AM) as matrix components. This process involves the free-radical polymerization of AM at 60 °C to form PAM[46]. As shown in Supplementary Figure 2, PANI reduces the aggregation or sedimentation of $CoFe_2O_4$, enabling its uniform dispersion within the hydrogel, which helps promote the formation and stability of the hydrogel pore structure. In addition, FT-IR analysis of the PG hydrogel [Figure 2I] showed

characteristic bands at 2,934, 1,415, and 1,037 cm^{-1}, corresponding to C-H stretching, O-H bending, and C-O stretching vibrations of glycerol, respectively[47], confirming the successful construction of the PG hydrogel.

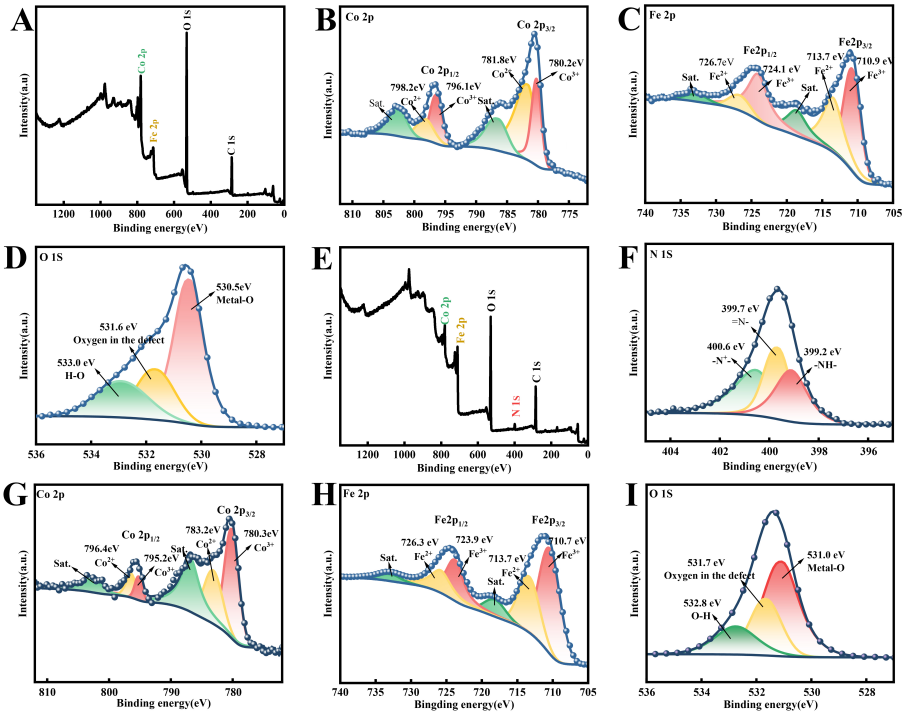

Figure 3. XPS characterization of $CoFe_2O_4$ and PANI@$CoFe_2O_4$. (A-D) Survey, Co 2p, Fe 2p, and O 1s spectra of $CoFe_2O_4$; (E-I) Survey, N 1s, Co 2p, Fe 2p, and O 1s spectra of PANI@$CoFe_2O_4$. XPS: X-ray photoelectron spectroscopy; PANI: polyaniline.

XPS analysis [Figure 3A] confirmed that spinel $CoFe_2O_4$ mainly consists of Co, Fe, and O, with no detectable impurities other than adventitious carbon. The high-resolution XPS spectra of Co 2p, Fe 2p, and O 1s are shown in Figure 3B-D. In Figure 3B, the two principal peaks at 780.5 and 796.6 eV are assigned to Co $2p_{3/2}$ and Co $2p_{1/2}$, respectively. The peaks at 780.2 and 796.1 eV correspond to Co^+, whereas those at 778.8 and 794.2 eV are attributed to Co^2[48,49]. The spectrum of Fe2p [Figure 3C] shows characteristic peaks at binding energies of 711.0 eV and 724.7 eV, corresponding to Fe $2p_{3/2}$ and Fe $2p_{1/2}$. The peaks at 710.9 eV and 724.1 eV are attributed to Fe^{3+}, while the peaks at 713.7 eV and 726.7 eV correspond to Fe^{2+}[48,50]. The O 1s XPS spectrum exhibits three characteristic peaks [Figure 3D]. The peak at 530.5 eV corresponds to the metal-oxygen bonds, while the peak at 531.6 eV is assigned to defect oxygen. The peak at 533.0 eV arises from adsorbed water molecules on the surface of $CoFe_2O_4$[50,51]. When coated with PANI, as shown in Figure 3E, it is evident that the PANI@$CoFe_2O_4$ composite nanoparticles contain an additional N element. The N 1s spectrum [Figure 3F] shows three peaks at binding energies of 399.2 eV, 399.7 eV, and 400.6 eV, which are attributed to imine nitrogen (=N-), amine nitrogen (-NH-), and protonated nitrogen ($-N^+-$)[52]. The binding energies of Co, Fe, and O in PANI@$CoFe_2O_4$ do not exhibit significant shifts [Figure 3G-I], suggesting that no new covalent bonds were formed between PANI and $CoFe_2O_4$ and that the two components were mainly integrated through interfacial interactions.

Physical properties of the hydrogel

The melting and crystallization behaviors of the hydrogels were investigated by differential scanning calorimetry. As shown in Figure 4A and B, the incorporation of functional fillers induced slight variations in the melting and crystallization behaviors of the hydrogel, which can be attributed to their influence on the microcrystalline domains and chain packing of the polymer network. In terms of mechanical performance,

PANI@$CoFe_2O_4$ acted as a multifunctional reinforcing filler, enhancing the mechanical properties of the organohydrogel through multiple interactions and structural effects. As shown in Figure 4C and D, the mechanical properties of the hydrogel were improved after incorporation of functional fillers. Among the samples investigated, the compressive strength (679.8 ± 13.60, n = 3) and modulus (1,258.9 ± 25.18, n = 3) of 4-PG/PANI hydrogel were significantly higher than those of PG hydrogel (376.3 ± 7.53 and 813.6 ± 16.27, n = 3, unpaired t-test, $P < 0.0001$, conformed to a normal distribution). Although both PANI and $CoFe_2O_4$ contributed to mechanical reinforcement, their strengthening mechanisms were different. The N- and O-containing functional groups on the PANI chains formed reversible physical crosslinking sites with the organohydrogel matrix, which helped maintain the integrity of the network under small deformation and partially dissociated or slid under large deformation to dissipate energy[19,53], thereby improving the elongation at break and toughness. In contrast, $CoFe_2O_4$ possesses a rigid structure with a mechanical modulus much higher than that of the soft polymer network. When uniformly dispersed within the hydrogel network, it can effectively bear and distribute external forces, thereby reducing local stress concentrations[54]. However, $CoFe_2O_4$ exhibits poor dispersibility within the hydrogel. Therefore, we introduced PANI onto its surface to overcome this limitation. When 4% PANI@$CoFe_2O_4$ filler is incorporated, the organohydrogel 4-PG/P@CoFe achieves a compressive strength (644.7 ± 25.89, n = 3) and modulus (1,076 ± 31.53, n = 3) that are significantly higher than those of PG hydrogel (376.3 ± 7.53 and 813.6 ± 16.27, n = 3, unpaired t-test, $P < 0.0001$, conformed to a normal distribution).The hydrogel's 3D cross-linked network structure not only endows it with excellent mechanical properties, such as toughness, elasticity, and fatigue resistance, but also ensures its outstanding water absorption and water retention capabilities. The storage of water molecules within its three-dimensional porous structure generally determines the stability of the hydrogel. Accordingly, the water retention capacity and water absorption performance of the glycerol-water binary system was quantitatively evaluated. Figure 4E demonstrates that the incorporation of glycerol exerts a significant enhancing effect on water retention capability. Under the same conditions, the hydrogel without glycerol exhibits a faster water loss rate than the glycerol-containing hydrogel. After 15 days of incubation under room temperature conditions, the water retention rate increases from 63.4 ± 0.75% to 77.1 ± 0.91%. Regarding the water absorption performance [Figure 4F], it can be observed that the hydrogel without glycerol exhibits a faster water uptake rate, indicating that water molecules permeate more rapidly in the glycerol-free system. Figure 4G shows a schematic diagram of the molecular chains moving relative to each other when the hydrogel is loaded. This further demonstrates that glycerol hinders the diffusion of water molecules. Therefore, the PG hydrogel can maintain its initial state and excellent performance over a longer period. Compared with conventional hydrogels, this improvement ensures the long-term preservation of structural integrity and functional performance. The surface of the PG/P@CoFe hydrogel contains abundant polar functional groups, enabling strong interfacial adhesion to various substrates, including biological tissues, inorganic glass, and plastics [Figure 4H]. Such robust adhesion provides a solid foundation for the integration of wearable sensors.

Electromagnetic shielding performance of the hydrogel

In general, EMI shielding originates from reflection, absorption, and multiple internal reflections, which are associated with the responses of mobile charge carriers, electric dipoles, and internal interfaces/surfaces[55,56]. Moreover, the porous structure not only reduces the density of the material but also provides a large surface area and abundant accessible active sites. These active sites facilitate the scattering or multiple reflections of electromagnetic waves (EMWs), thereby promoting energy dissipation[57,58]. Meanwhile, the three-dimensional network structure increases the probability that the incident electromagnetic waves undergo multiple reflections and attenuation. As shown in Figure 5A-D, the hydrogels exhibit efficient and stable EMI shielding performance in the X-band, with the EMI shielding effectiveness increasing as the frequency rises. This variation can be attributed to several factors. (1) Enhanced dipole absorption: Water molecules possess a large permanent dipole moment, and under an alternating electromagnetic field, they

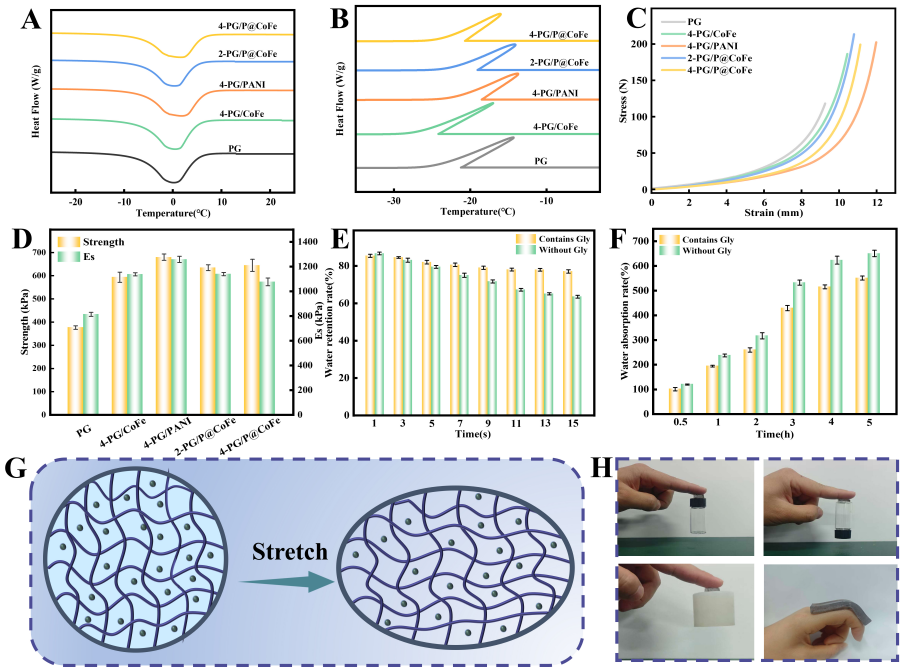

Figure 4. Physical properties of the hydrogels. (A and B) Crystallization and crystallization curves of the hydrogel; (C) Compression curve of hydrogel; (D) Compression strength and compression modulus of the hydrogel; (E and F) Effect of Gly on the water retention and water absorption rates of the hydrogel; (G) Schematic of the semi-interpenetrating network changes of the hydrogel during stretching; (H) Images of the hydrogel's adhesion to different objects. Data are presented as mean ± SD (n = 3); error bars represent standard deviation. All photos in the figure were taken by the author during the experiment. PG: Polyacrylamide/glycerol; SD: standard deviation; PANI: polyaniline

undergo continuous orientational polarization. This process leads to stronger attenuation of interfering electromagnetic waves within the hydrogel, thereby dissipating the electromagnetic energy in the form of heat[57]. (2) Increased polarization relaxation: At higher frequencies, the electromagnetic field oscillates more rapidly, causing more frequent polarization relaxation of electric dipoles, which in turn enhances conduction loss[59]. More intense reflection and scattering: The shorter wavelengths associated with high-frequency electromagnetic waves interact more readily with the electric dipoles of water molecules and are more effectively reflected and scattered within the porous structure of the hydrogel, thereby generating greater energy dissipation[60]. As can be seen from Supplementary Figure 3, the electromagnetic shielding performance of hydrogels filled with the composite material formed by PANI and $CoFe_2O_4$ is superior to that filled with the two components separately. The reason is that PANI coating can reduce the sedimentation of $CoFe_2O_4$ at the bottom of the hydrogel. Although water has a strong ability to dissipate electromagnetic waves, the pure PG hydrogel cannot achieve a satisfactory SE value due to the absence of conductive and magnetic components. This indicates the necessity of incorporating conductive and magnetic components into the PG hydrogel to achieve high electromagnetic shielding performance. As shown in Figure 5E, the electrical conductivity of the hydrogel changes significantly after the incorporation of the composite material. The electrical conductivity (0.55 ± 0.01, n = 3) and compressive performance (50.27 ± 2.51, n = 3) of 4-PG/P@CoFe hydrogel were significantly higher than those of PG hydrogel (0.0648 ± 0.00389 and 17.51 ± 1.05, n = 3, unpaired t-test, $P < 0.0001$, conformed to a normal distribution). Although the PG/PANI hydrogel exhibits higher electrical conductivity than the 2-PG/P@CoFe hydrogel, its shielding performance relies primarily on free-electron reflection. Due to the absence of dielectric polarization, interfacial polarization, and magnetic loss-related absorption mechanisms, its overall shielding effectiveness remains limited[61]. In contrast, the 4-PG/P@CoFe hydrogel exhibits a moderately reduced conductivity while significantly enhancing impedance matching, dielectric loss, magnetic loss, and multiple scattering. This

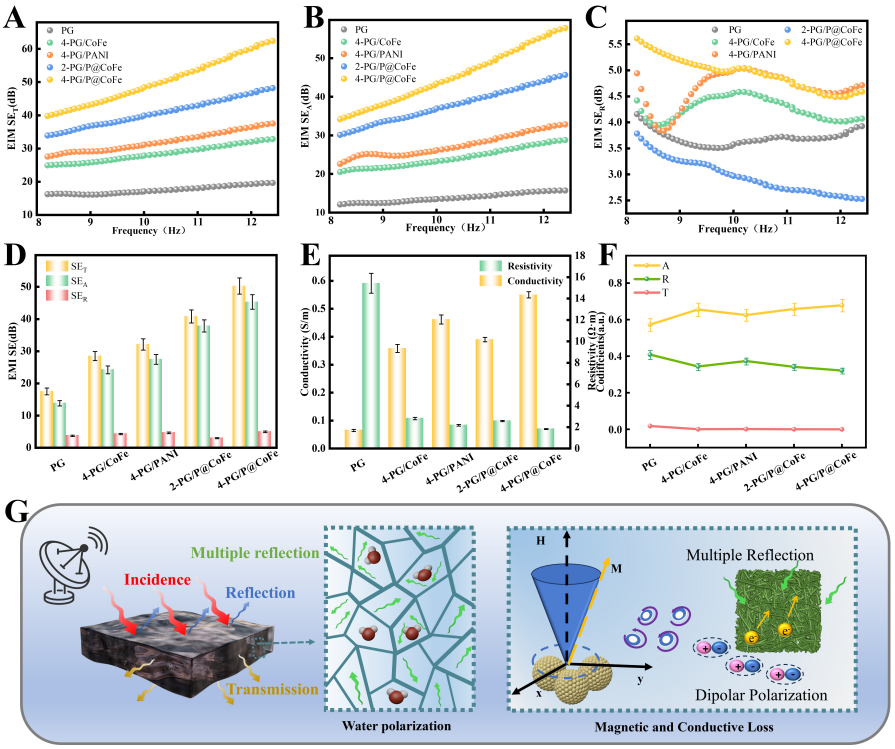

Figure 5. Electromagnetic shielding performance of the hydrogels. (A-C) Clearly illustrate the influence of frequency on the SET, SER, and SEA of the hydrogels; (D) Average SET, SER, and SEA values of hydrogels; (E) Electrical conductivity of the hydrogels; (F) T-R-A coefficients of the hydrogels; (G) Electromagnetic shielding mechanism of the hydrogels. Data are presented as mean ± SD (n = 3); error bars represent standard deviation. PG: Polyacrylamide/glycerol; SET: total shielding effectiveness; SER: reflection shielding effectiveness; SEA: absorption shielding effectiveness; SD: standard deviation.

results in an absorption-dominated shielding mechanism, leading to electromagnetic shielding performance far superior to that of the 4-PG/PANI hydrogel. The present results suggest that simply increasing conductivity does not necessarily improve EMI shielding performance. A possible reason is that excessively high conductivity may deteriorate impedance matching, thereby increasing surface reflection[62]. As shown in Figure 5F, by analyzing the R, A and T coefficients, we can gain additional understanding of the shielding mechanism. It can be observed that the 4-PG/PANI hydrogel exhibits slightly higher R values than the other samples due to its relatively strong dielectric properties, which lead to increased impedance mismatch. More importantly, the T values of all hydrogels are close to zero, indicating their high efficiency in resisting electromagnetic interference[63,64]. Meanwhile, the A values are consistently higher than the R values, indicating that absorption is the dominant EMI shielding mechanism[65]. The schematic illustration of the electromagnetic shielding mechanism [Figure 5G] further demonstrates the EMI shielding process of the hydrogel. Table 1 Comparison of the electromagnetic shielding performance of this work with other multifunctional hydrogels[5,11,27,66-72].

Infrared stealth performance of the hydrogel

To meet the demands of more complex environments, we further evaluated the infrared stealth performance of the hydrogels. Hydrogels containing different fillers were placed on an 80 °C heating plate for 20 min, and their surface temperatures were recorded at various time intervals using an infrared thermal imaging camera. As shown in Figure 6A, the surface temperature of the hydrogel gradually increases with time. After 15 min, the equilibrium radiation temperature of the PG hydrogel stabilizes at approximately 45 °C, which is about 35 °C lower than the heating plate. This indicates that hydrogel exhibits a noticeable thermal-insulation effect. This phenomenon may be attributed to the following factors. (1) The presence of glycerol in the

Table 1. Comparison of the EMI shielding performance of representative hydrogels

Sample	Thick (mm)	EMI SE	References
MXene/$CoFe_2O_4$ hydrogel	5 mm	54.21 dB	[5]
MXene@COF hydrogel	3 mm	32.01	[11]
Fe_3O_4@RGO/PAM hydrogel	3 mm	27.10 dB	[27]
MXene Organohydrogel	4 mm	32.8 dB	[66]
MXene/gelatin hydrogel	3-5 mm	35–50 dB	[67]
MXene /PAM-CMC hydrogel	5 mm	46.3 dB	[68]
PVA-ANF/MXene@Ga hydrogel	/	35.7 dB	[69]
PVA/PAA@PEGDMA/ PEDOT:PSS hydroge	4 mm	40.61 dB	[70]
MXene/PEDOT:PSS hydrogels	4.5 mm	41 dB	[71]
ANE hydrogel	4 mm	31.5 dB	[72]
4-PG/P@CoFe Organohydroge	4 mm	50.27 dB	This Work

EMI SE: Electromagnetic interference shielding effectiveness; COF: covalent organic framework; PAM: polyacrylamide; CMC: PVA: ANF: PAA: EGDMA: PEDOT:PSS: ANE:

hydrogel slows down the evaporation rate of water and promotes the formation of a dense and stable hydrogen-bonding network within the three-dimensional gel matrix. This significantly hinders heat transfer during conduction, thereby imparting the material with a low thermal conductivity[65,73]. (2) The three-dimensional microscopic network structure of the hydrogel suppresses convective heat transfer between the material and the surrounding air[73]. It is the synergistic effect of these factors that effectively suppresses heat conduction and convection, thereby slowing the temperature rise and enabling excellent infrared stealth performance. However, it is noteworthy that after the incorporation of fillers [Figure 6B-E], the heating rate of the hydrogels increases, and the surface reaches its equilibrium radiation temperature within approximately 10 min. This is because of the contact or close packing between fillers form thermal bridges, creating continuous heat-transfer pathways that allow heat to penetrate the material more easily. However, because the heat-source intensity and surface heat-dissipation conditions remain unchanged, the system ultimately reaches thermal equilibrium at the same heat-flux balance point. As a result, the equilibrium radiation temperature shows only minor variation.

To better simulate the practical application scenario, the hydrogel was applied to the palm. As shown in Figure 6F, the infrared signal of the bare palm exhibited a distinct color contrast relative to the surrounding background. In contrast, the region covered by the hydrogel blended well with the environment and displayed a thermal signature similar to that of the surroundings, demonstrating the excellent infrared stealth capability of the hydrogel. Figure 6G and H respectively show the change in hydrogel surface temperature over time and the infrared stealth mechanism.

Sensing performance of the hydrogel

As shown in Supplementary Figure 4, the gauge factor (GF) of 4-PG/P@CoFe exhibits a value of 2.88 over a 0%-100% strain range, demonstrating excellent linearity (R^2 = 0.997). This linear response is attributed to the PANI@$CoFe_2O_4$ nanoparticles, which, as conductive materials embedded within the organohydrogen network, effectively maintain the continuity of the conductive pathways under applied strain. The 4-PG/P@CoFe hydrogel, with its excellent mechanical properties, electrical conductivity, and adhesion, is highly suitable for real-time sensing and monitoring of human motion and health conditions. As shown in Figure 7, the 4-PG/P@CoFe hydrogel exhibits good linearity and sensitivity, enabling real-time detection of various strains and resistance signals generated under different motion states. It can capture subtle facial

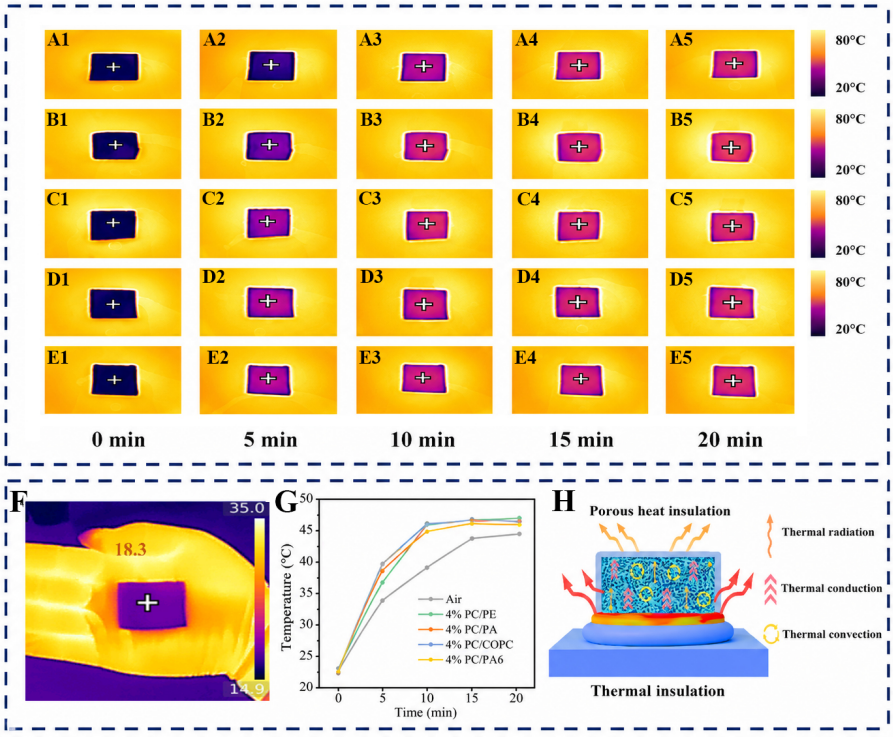

Figure 6. Evaluation of the samples' infrared stealth capabilities. (A-E) Infrared thermal images of the hydrogel samples placed on a heating plate maintained at 80 °C. (F) Infrared thermal image of the 4-PG/P@CoFe hydrogel; (G) Temperature-time curves of the sample surfaces; (H) Thermal insulation mechanism of hydrogel. PG: Polyacrylamide/glycerol.

expressions in other areas, such as frowning [Figure 7A] and changes in mouth shape [Figure 7B]. When fixed on the throat [Figure 7C], the vibrations of the Adam's apple can be detected as we shout the words 'Bing Dun Dun', resulting in a clear and regular waveform output. Due to the Poisson effect of the hydrogel, different bending amplitudes generate distinct and regular electrical signals, as varying degrees of stretching induce different levels of network contraction and resistance change[74]. The signal intensity correlates with the magnitude of movement, enabling precise motion detection. Furthermore, the hydrogel was used to track joint motion. Figure 7D-F shows the electrical signals obtained from finger, wrist, elbow, and knee bending at various angles. These results further confirm the rapid response capability and signal stability of the 4-PG/P@CoFe hydrogel sensor under dynamic, real-time monitoring conditions. The outstanding sensing performance of the 4-PG/P@CoFe hydrogel provides a solid functional foundation for its potential applications in human motion monitoring, health management, and gesture recognition.

CONCLUSION

In summary, a multifunctional PG/P@CoFe organohydrogel was successfully fabricated by integrating conductive-magnetic PANI@$CoFe_2O_4$ nanoparticles into a PAM/Gly hydrogel network through a hydrothermal-assisted one-pot strategy. The obtained hydrogel exhibited excellent compressive properties and enhanced water-retention capability due to the incorporation of glycerol. Electromagnetic measurements revealed that, at a PANI@$CoFe_2O_4$ filler content of 4 wt.%, the 4 mm-thick hydrogels achieved an electrical conductivity of 0.55 ± 0.01 S/m and an average EMI shielding effectiveness of 50.27 ± 2.51 dB in the X-band. In addition, the hydrogel demonstrated excellent thermal insulation performance, together with favorable adhesion and rapid strain-responsive behavior for human-motion monitoring. This work provides an effective strategy for the development of integrated flexible materials combining strain sensing, electromagnetic shielding, and thermal management. With its multifunctionality and outstanding

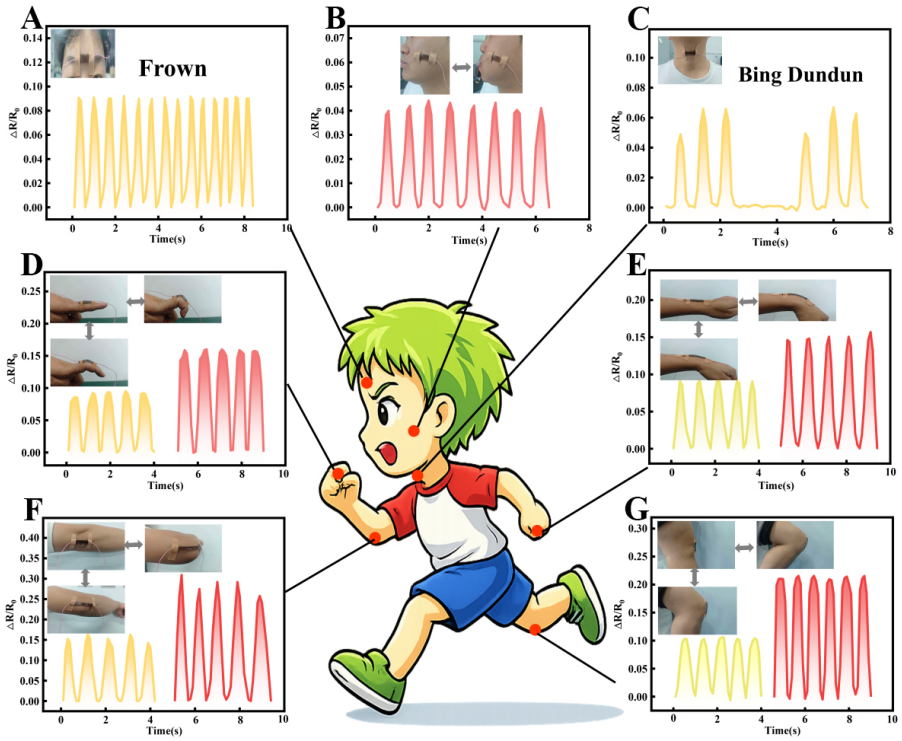

Figure 7. Real-time human-motion and physiological-signal monitoring using the 4-PG/P@CoFe hydrogel sensor. (A)Frowning; (B) Cheek puffing; (C) Throat vocalization; (D) Finger bending at different angles; (E) Wrist bending at different angles; (F) Elbow flexion at different angles; (G) Knee bending at different angles. All photos in the figure were taken by the author during the experiment. PG: Polyacrylamide/glycerol.

electromagnetic shielding performance, the hydrogel holds significant potential for applications in wearable electronic devices.

DECLARATIONS

Authors' contributions

Validation: Lei, Z.
Writing - original draft: Lei, Z.; Lu, M.
Writing - review & editing: Lei, Z.; Zhang, D.; Wang, J.; Dong, W.
Data curation: Lu, M.; Liu, D.; Hu, Y.; Song, A.
Funding acquisition: Zhang, D.; Wang, J.; Dong, W.

Availability of data and materials

The data are available from the corresponding authors upon reasonable request.

AI and AI-assisted tools statement

The image of the running boy in Figure 7 was generated with the assistance of an AI-based tool and was further revised and optimized by the authors.

Financial support and sponsorship

This study was financially supported by the National Natural Science Foundation of China Project (52163001), Guizhou Provincial Science and Technology Plan Project (Qiankehe Platform Talent-GCC[2022]010-2, Qiankehe Zhongyindi [2024]042, Qiankehe Jichu-ZK[2024]YB488, Qiankehe Zhongyindi (2025)013, Qiankehe Results [2025]109,Qiankehe Talent XKBF(2025)005), Guizhou Provincial Scientist Workstation (Qiankehe Platform KXJZ[2024]022), Guizhou Provincial Department of Education 'Hundred Universities, Thousand Enterprises Science and Technology Challenge Project' (Qian Jiao Ji [2025] No. 007), Doctor Startup Fund of Guizhou Minzu University (Grant No.GZMUZK[2024]QD77).

Conflicts of interest

All authors declared that there are no conflicts of interest.

Ethical approval and consent to participate

This study only conducted non-invasive data collection through simply placing the device on the skin, and does not involve invasive procedures or human health risks. According to Article 32 of the "Measures for the Ethical Review of Life Science and Medical Research Involving Human Subjects (Trial)", this study meets the conditions for exemption from review. All participants participated in the experiment with informed consent.

Consent for publication

Not applicable.

Copyright

Supplementary Materials

Supplementary Materials

REFERENCES

1. He, M.; Zhong, X.; Lu, X.; et al. Excellent low-frequency microwave absorption and high thermal conductivity in polydimethylsiloxane composites endowed by hydrangea-like CoNi@BN heterostructure fillers. *Adv. Mater.* **2024**, *36*, 2410186. DOI
2. Hao, Y.; Liu, C.; Keram, R.; Song, H.; Zhang, Y.; Ji, G. Machine-learning assisted novel insulation layer stripping technology for upgrading the transparent EMI shielding materials. *Nano. Today.* **2025**, *61*, 102660. DOI
3. Panahi-Sarmad, M.; Samsami, S.; Ghaffarkhah, A.; et al. MOF-based electromagnetic shields multiscale design: nanoscale chemistry, microscale assembly, and macroscale manufacturing (Adv. Funct. Mater. 43/2024). *Adv. Funct. Mater.* **2024**, *34*, 2470254. DOI
4. Li, Y.; Han, X.; Zhu, J.; Feng, Y.; Liu, P.; Chen, X. MOF-derived Co/C-anchored MoS_2-based phase change materials toward thermal management and microwave absorption. *Electron* **2024**, *2*, e56. DOI
5. Wang, L.; Jiang, Y.; Liu, Y.; et al. Multifunctional hydrogels based on MXene/$CoFe_2O_4$ synergistically assisted rapid gelation for electromagnetic shielding, infrared stealth and wearable sensors. *Chem. Eng. J.* **2025**, *521*, 167172. DOI
6. Xie, X.; Lu, M.; Li, G.; et al. Anti-impact electromagnetic shielding hydrogel with solvent-driven tunability. *Chem. Eng. J.* **2025**, *505*, 159114. DOI
7. Feng, Y.; Qin, M.; Qin, J.; et al. Synergistic thermal management and electromagnetic wave absorption in core-sheath phase change composites. *Adv. Funct. Mater.* **2025**, *36*, e23075. DOI
8. Liu, Q.; Wang, P.; Zhang, W.; et al. Multifunctional wood-derived cellulose/$Ti_3C_2T_x$ composite films enhanced by densification strategy for electromagnetic shielding, Joule/solar heating, and thermal camouflage. *Chem. Eng. J.* **2024**, *493*, 152696. DOI
9. Zhou, T.; Zhang, D.; Diao, K.; et al. Constructing PAM/PEG electromagnetic shielding hydrogels based on MWCNTs@TiO_2. *Mater. Today. Nano.* **2025**, *29*, 100606. DOI
10. Chen, Y.; Guo, W.; Chen, N.; et al. Skin-inspired MXene-based polyvinyl alcohol/gelatin organic hydrogel with good anti-drying, anti-swelling properties and high sensitivity. *Sensor. Actuat. A-Phys.* **2025**, *383*, 116231. DOI
11. Diao, K. L.; Zhang, D. H.; Du, J. J.; Zhou, T.; Liu, D. J.; Qin, S. H. Electromagnetic shielding and thermal insulation hydrogels were constructed based on covalent organic skeleton COF and $Ti_3C_2T_x$ MXene. *Rare. Metals.* **2025**, *44*, 7738-50. DOI
12. Xu, Y.; Zhan, X.; Du, J.; Wu, Z.; Zhang, D. Fluorescent hydrogel with high toughness response based on lanthanide metals: material adhesion, multicolor modulation, information encryption. *Chem. Eng. J.* **2024**, *489*, 151303. DOI
13. Ma, N.; Chen, Y.; Wang, L.; et al. Ag/AgCl@agar/P(AM-co-HEAA) hydrogel with ultra-stretchability, fatigue resistance, and freezing tolerance for human motion and electrophysiological signal monitoring. *Int. J. Biol. Macromol.* **2025**, *331*, 148239. DOI
14. He, T.; Liu, C.; Chen, Z.; et al. Multi-layer alternating structured alginate hydrogels featuring exceptional flexibility and electromagnetic shielding performance. *J. Colloid. Interface. Sci.* **2025**, *699*, 138103. DOI
15. Arunprasath, K.; Senthamaraikannan, P.; Suyambulingam, I.; et al. Comprehensive review of advances in natural fiber composites for conductive and EMI shielding applications: Materials, mechanisms, and future prospects. *Int. J. Biol. Macromol.* **2025**, *320*, 145892. DOI
16. Chi, J.; Gu, S.; Shi, R.; et al. Extending PANI molecular chains into pores of hierarchical MIL-101 as flexible electrodes for supercapacitor applications. *Chem. Eng. J.* **2025**, *510*, 161764. DOI

17. Cao, G.; Wu, A.; Wang, Z.; Zhong, S.; Cao, Z.; Zhang, H. Enhancing the conductivity and dispersion properties of polyaniline using ethyl orange. *Colloid. Surface. A.* **2025**, *704*, 135489. DOI
18. Kandpal, R., Shahadat, M., Adnan, R., Ali, S. W., Ahammad, S. Z. Polyaniline-based flexible nanocomposite materials. In *Biorenewable Nanocomposite Materials, Vol. 1: Electrocatalysts and Energy Storage*; Pathania, D., Singh, L., Eds.; ACS Symposium Series, Vol. 1410; American Chemical Society, 2022; pp 367-95. DOI
19. Zhao, L.; Tang, N.; Wang, X.; Li, M.; Hu, J. Conductive polyaniline hydrogel featuring high toughness and low hysteresis. *Chin. J. Polym. Sci.* **2025**, *43*, 581-7. DOI
20. Mahdy, M. A.; Azab, A. A.; El Zawawi, I. K.; Turky, G. Tailoring ZnO/$CoFe_2O_4$ nanocomposites: structure, optical, dielectric and magnetic study. *Phys. Scr.* **2022**, *98*, 015806. DOI
21. Gholipur, R. Preparation and electromagnetic waves absorption performance of novel peanut shell/$CoFe_2O_4$/$(RGO)_x$/PVA nanocomposites. *Sci. Rep.* **2024**, *14*, 30699. DOI
22. Abraime, B.; El Maalam, K.; Fkhar, L.; et al. Influence of synthesis methods with low annealing temperature on the structural and magnetic properties of $CoFe_2O_4$ nanopowders for permanent magnet application. *J. Magn. Magn. Mater.* **2020**, *500*, 166416. DOI
23. Asandulesa, M.; Hamciuc, C.; Pui, A.; et al. Cobalt ferrite/polyetherimide composites as thermally stable materials for electromagnetic interference shielding uses. *Int. J. Mol. Sci.* **2023**, *24*, 999. DOI PubMed PMC
24. Bastianello, M.; Gross, S.; Elm, M. T. Thermal stability, electrochemical and structural characterization of hydrothermally synthesised cobalt ferrite ($CoFe_2O_4$). *RSC. Adv.* **2019**, *9*, 33282-9. DOI PubMed PMC
25. Saleem, S.; Irfan, M.; Naz, M. Y.; et al. Investigating the impact of Cu^{2+} doping on the morphological, structural, optical, and electrical properties of $CoFe_2O_4$ nanoparticles for use in electrical devices. *Materials* **2022**, *15*, 3502. DOI
26. Afzia, M.; Khan, R. A.; Ismail, B.; et al. Correlation between magnetic and dielectric response of $CoFe_2O_4$:Li^{1+}/Zn^{2+} nanopowders having improved structural and morphological properties. *Molecules* **2023**, *28*, 2824. DOI
27. Zhou, T.; Zhan, X.; Diao, K.; et al. RGO loaded Fe_3O_4 strategy to construct high toughness PAM hydrogel for electromagnetic shielding. *Prog. Org. Coat.* **2024**, *196*, 108750. DOI
28. Su, J.; Dong, X.; Zhao, H.; et al. Dual-loss mechanisms in low-filler CoFe@$CoFe_2O_4$/biomass carbon composites for enhanced microwave absorption. *Colloid. Surface. A.* **2025**, *726*, 137953. DOI
29. Gao, Y.; Chen, X.; Jin, X.; et al. Multifunction integration within magnetic CNT-bridged MXene/CoNi based phase change materials. *eScience* **2024**, *4*, 100292. DOI
30. Wang, J.; Wu, W.; Zhang, W.; et al. Synthesis, electrical conductivity, and wave-absorption performances of bamboo-based composites co-doped with graphene oxide and polyaniline. *Polymers* **2024**, *17*, 78. DOI PubMed PMC
31. Zhao, M.; Ran, S.; Guo, X.; et al. Magnetic-dielectric synergy in Fe_3O_4/MoS_2@polyaniline composites for high-efficiency electromagnetic wave absorption and corrosion resistance. *J. Alloys. Compd.* **2025**, *1048*, 185300. DOI
32. Almeida, A. I. D. R.; Carvalho, L. D. O.; Lopes, R. C.; et al. Enhanced polyacrylamide polymer hydrogels using nanomaterials for water shutoff: morphology, thermal and rheological investigations at high temperatures and salinity. *J. Mol. Liq.* **2024**, *405*, 125041. DOI
33. Son, D.; Hwang, H.; Fontenot, J. F.; Lee, C.; Jung, J. P.; Kim, M. Tailoring physical properties of dual-network acrylamide hydrogel composites by engineering molecular structures of the cross-linked network. *ACS. Omega.* **2022**, *7*, 30028-39. DOI PubMed PMC
34. Li, G.; Liu, Y.; Chen, Y.; et al. Robust, self-adhesive, and low-contact impedance polyvinyl alcohol/polyacrylamide dual-network hydrogel semidry electrode for biopotential signal acquisition. *SmartMat* **2023**, *5*, e1173. DOI
35. Liaskovska, M. Adsorption properties of magnetic $CoFe_2O_4$ based spinel nanoparticles. In *Nanomaterials and Nanocomposites, Nanostructures, and Their Applications*; Fesenko, O., Yatsenko, L., Eds.; Springer Proceedings in Physics, Vol. 253; Springer Nature Switzerland, 2024; pp 171-84. DOI
36. Yun, T.; Kim, H.; Iqbal, A.; et al. Electromagnetic shielding of monolayer MXene assemblies. *Adv. Mater.* **2020**, *32*, 1906769. DOI
37. Xia, Y.; Gao, W.; Gao, C. A review on graphene-based electromagnetic functional materials: electromagnetic wave shielding and absorption. *Adv. Funct. Mater.* **2022**, *32*, 2204591. DOI
38. Adamiak, K.; Sionkowska, A. State of innovation in alginate-based materials. *Marine. Drugs.* **2023**, *21*, 353. DOI PubMed PMC
39. Wurm, F.; Rietzler, B.; Pham, T.; Bechtold, T. Multivalent ions as reactive crosslinkers for biopolymers - a review. *Molecules* **2020**, *25*, 1840. DOI
40. Sharma, D.; Kaith, B. S.; Rajput, J. Single step *in situ* synthesis and optical properties of polyaniline/ZnO nanocomposites. *Sci. World. J.* **2014**, *2014*, 1-13. DOI
41. Butoi, B.; Groza, A.; Dinca, P.; Balan, A.; Barna, V. Morphological and structural analysis of polyaniline and poly(o-anisidine) layers generated in a DC glow discharge plasma by using an oblique angle electrode deposition configuration. *Polymers* **2017**, *9*, 732. DOI PubMed PMC

42. Zawrah, M.; El-Okr, M.; Ashery, A.; Abou Hammad, A. Characterization of sol-gel fabricated cobalt ferrite $CoFe_2O_4$ nanoparticles,. *Middle. East. J. Appl. Sci.* **2016**, *6*, 362-6. Available from: https://www.curresweb.com/mejas/mejas/2016/362-366.pdf.
43. To Loan, N. T.; Hien Lan, N. T.; Thuy Hang, N. T.; et al. $CoFe_2O_4$ nanomaterials: effect of annealing temperature on characterization, magnetic, photocatalytic, and photo-Fenton properties. *Processes* **2019**, *7*, 885. DOI
44. Jamil, M.; Ahmad, J.; Bukhari, S.; et al. Effect on structural and optical properties of Zn-substituted cobalt ferrite $CoFe_2O_4$,. *J. Ovonic. Res.* **2017**, *13*, 45-53. Available from: https://chalcogen.ro/45_JamilMT.pdf.
45. Kumar, S.; Ahmed, F.; Shaalan, N. M.; et al. Structural, magnetic, and electrical properties of $CoFe_2O_4$ nanostructures synthesized using microwave-assisted hydrothermal method. *Materials* **2022**, *15*, 7955. DOI
46. Peng, R.; Luo, Y.; Cui, Q.; Zhang, H.; Li, L. Covalent organic frameworks as efficient photoinitiators and cross-linkers to fabricate highly stretchable hydrogels. *ACS. Appl. Mater. Interfaces.* **2022**, *14*, 49254-63. DOI
47. Sivaselvam, S.; Selvakumar, R.; Viswanathan, C.; Ponpandian, N. Rapid one-pot synthesis of PAM-GO-Ag nanocomposite hydrogel by gamma-ray irradiation for remediation of environment pollutants and pathogen inactivation. *Chemosphere* **2021**, *275*, 130061. DOI
48. Liu, Q.; Kang, X.; Xing, L.; Ye, Z.; Yang, Y. A facile synthesis of nanostructured $CoFe_2O_4$ for the electrochemical sensing of bisphenol A. *RSC. Adv.* **2020**, *10*, 6156-62. DOI PubMed PMC
49. Jiang, H.; Feng, Z.; Liu, K.; Wang, H.; Lin, J. Constructing interconnected $CoFe_2O_4$/CoFe alloyed nanosheets for efficient oxygen evolution reaction. *SSRN* **2025**. DOI
50. Qu, Q.; Chen, Z.; Sun, G.; Qiu, L.; Zhu, M. $CoFe_2O_4$ nanoparticles as a bifunctional agent on activated porous carbon for battery-type asymmetrical supercapacitor. *Chem. Synth.* **2024**, *4*, 26. DOI
51. Rehman, W.; Saeed, F.; Zhao, Y.; et al. Boosted photoelectrochemical water oxidation performance with a quaternary heterostructure: $CoFe_2O_4$/MWCNT-Doped MIL-100(Fe)/TiO_2. *Catalysts* **2024**, *14*, 901. DOI
52. Smolin, Y. Y.; Soroush, M.; Lau, K. K. S. Oxidative chemical vapor deposition of polyaniline thin films. *Beilstein. J. Nanotechnol.* **2017**, *8*, 1266-76. DOI PubMed PMC
53. Yang, J.; Yu, X.; Sun, X.; et al. Polyaniline-decorated supramolecular hydrogel with tough, fatigue-resistant, and self-healable performances for all-in-one flexible supercapacitors. *ACS. Appl. Mater. Interfaces.* **2020**, *12*, 9736-45. DOI
54. Dellatolas, I.; Bantawa, M.; Damerau, B.; et al. Local mechanism governs global reinforcement of nanofiller-hydrogel composites. *ACS. Nano.* **2023**, *17*, 20939-48. DOI
55. Zhou, H.; Cao, W.; Sun, N.; Jiang, L.; Liu, Y.; Pang, H. Formation mechanism and properties of NiCoFeLDH@ZIF-67 composites. *Chin. Chem. Lett.* **2021**, *32*, 3123-7. DOI
56. Liu, C.; Zhu, L.; Zheng, S.; et al. A novel elastic dome array structure for precise pressure regulation toward tunable microwave absorption. *Acta. Mater.* **2025**, *296*, 121255. DOI
57. Zeng, Z.; Jin, H.; Chen, M.; Li, W.; Zhou, L.; Zhang, Z. Lightweight and anisotropic porous MWCNT/WPU composites for ultrahigh performance electromagnetic interference shielding. *Adv. Funct. Mater.* **2015**, *26*, 303-10. DOI
58. Feng, Y.; Hai, G.; Sun, G.; et al. Dual-functional phase change composites integrating thermal buffering and electromagnetic wave absorption via multi-interfacial engineering. *Adv. Fiber. Mater.* **2025**, *7*, 1873-87. DOI
59. Song, W.; Ness, S.; Desai, M.; Yi, J. Visible light optical coherence tomography angiography (vis-OCTA) in human retina for small vessel blood oxygenation (Conference Presentation). In *Ophthalmic Technologies XXX*, San Francisco, United States, February 1-6, 2020; Manns, F., Söderberg, P. G., Ho, A., Eds.; SPIE, 2020, pp 9. DOI
60. Ouyang, W.; Mei, L.; Liu, Q.; et al. Ultrathin-flexible multifunctional MXene composite hydrogels with good mechanical properties-high strain sensitivity and ultra-broadband EMI shielding performances. *Chem. Eng. J.* **2024**, *494*, 153068. DOI
61. Saeedi, F.; Ansari, R.; Sahmani, S. Recent advances and comprehensive review of electromagnetic interference shielding materials and technologies. *Mater. Today. Phys.* **2025**, *59*, 101917. DOI
62. Xiong, C.; Xiong, Q.; Zhao, M.; Wang, B.; Dai, L.; Ni, Y. Recent advances in non-biomass and biomass-based electromagnetic shielding materials. *Adv. Compos. Hybrid. Mater.* **2023**, *6*, 205. DOI
63. Zeng, Z.; Wang, C.; Siqueira, G.; et al. Nanocellulose-MXene biomimetic aerogels with orientation-tunable electromagnetic interference shielding performance. *Adv. Sci.* **2020**, *7*, 2000979. DOI
64. Zhang, Y.; Ruan, K.; Zhou, K.; Gu, J. Controlled distributed $Ti_3C_2T_x$ hollow microspheres on thermally conductive polyimide composite films for excellent electromagnetic interference shielding. *Adv. Mater.* **2023**, *35*, 2211642. DOI
65. Liu, H.; Yang, Y.; Tian, N.; You, C.; Yang, Y. Foam-structured carbon materials and composites for electromagnetic interference shielding: design principles and structural evolution. *Carbon* **2024**, *217*, 118608. DOI
66. Yu, Y.; Yi, P.; Xu, W.; et al. Environmentally tough and stretchable MXene organohydrogel with exceptionally enhanced electromagnetic interference shielding performances. *Nano-Micro. Lett.* **2022**, *14*, 77. DOI PubMed PMC

67. Zhou, X.; Ye, X.; Zhu, J.; Wang, G. Anti-drying, anti-freezing and super-elastic MXene/gelatin hydrogels for electromagnetic shielding and pressure sensing. *Mater. Today. Phys.* **2025**, *53*, 101709. DOI
68. Li, Y.; Xuan, X.; Pan, Z.; et al. A robust and multifunctional conductive double-network hydrogel exhibiting self-healing, anti-freezing, antibacterial, and electromagnetic shielding properties for advanced wearable sensors and biofabrication. *Chem. Eng. J.* **2025**, *522*, 167264. DOI
69. Shen, M.; Liang, C.; Xu, X.; et al. Liquid metal-enhanced PVA-ANF/MXene hydrogels for electromagnetic shielding and sensing. *ACS. Appl. Nano. Mater.* **2024**, *7*, 22158-68. DOI
70. Zhang, Z.; Liu, G.; Wu, J.; Jiang, X.; Liu, H.; Li, Z. High-strength dual-network hydrogels with chain-growth enhancement for multifunctional flexible sensors, triboelectric nanogenerators, and EMI shielding. *Chem. Eng. J.* **2025**, *519*, 165710. DOI
71. Li, P.; Wang, H.; Ju, Z.; et al. Ti_3C_2Tx MXene- and sulfuric acid-treated double-network hydrogel with ultralow conductive filler content for stretchable electromagnetic interference shielding. *ACS. Nano.* **2024**, *18*, 2906-16. DOI
72. Hao, J.; Hu, S.; Liu, D.; et al. 3D-printed multifunctional hydrogel for integrated electromagnetic interference shielding, infrared stealth, and wearable sensing. *ACS. Appl. Mater. Interfaces.* **2025**, *17*, 68525-38. DOI
73. Li, Y.; Cheng, Q.; Deng, Z.; et al. Recent progress of anti-freezing, anti-drying, and anti-swelling conductive hydrogels and their applications. *Polymers* **2024**, *16*, 971. DOI PubMed PMC
74. Yang, J.; Wang, B.; Zhao, Q.; et al. Sustainable conductive organohydrogel strengthened by lignin@polypyrrole core-shell nanoparticles for multifunctional wearable electronics. *SusMat* **2025**, *5*, e70027. DOI